View metadata, citation and similar papers at core.ac.uk
brought to you by CORE
provided by DSpace@MIT

Metrology for electron-beam lithography and resist contrast at the sub-10 nm scale

Huigao Duan[a)]
Department of Electrical Engineering and Computer Science, Massachusetts Institute of Technology, Cambridge, Massachusetts 02139 and School of Physical Science and Technology, Lanzhou University, Lanzhou, Gansu 730000, People's Republic of China

Vitor R. Manfrinato, Joel K. W. Yang,[a)] Donald Winston,
Bryan M. Cord, and Karl K. Berggren[b)]
Department of Electrical Engineering and Computer Science, Massachusetts Institute of Technology, Cambridge, Massachusetts 02139

(Received 23 July 2010; accepted 13 September 2010; published 22 November 2010)

Exploring the resolution limit of electron-beam lithography is of great interest both scientifically and technologically. However, when electron-beam lithography approaches its resolution limit, imaging and metrology of the fabricated structures by using standard scanning electron microscopy become difficult. In this work, the authors adopted transmission-electron and atomic-force microscopies to improve the metrological accuracy and to analyze the resolution limit of electron-beam lithography. With these metrological methods, the authors found that sub-5 nm sparse features could be readily fabricated by electron-beam lithography, but dense 16 nm pitch structures were difficult to yield. Measurements of point- and line-spread functions suggested that the resolution in fabricating sub-10 nm half-pitch structures was primarily limited by the resist-development processes, meaning that the development rates depended on pattern density and/or length scale. © *2010 American Vacuum Society.* [DOI: 10.1116/1.3501359]

I. INTRODUCTION

The continued miniaturization of devices requires high-resolution nanofabrication techniques and processes. Electron-beam lithography (EBL) is an industrially well-established nanofabrication method and has been widely used in bit-patterned media,[1] high-resolution templated self-assembly,[2,3] sub-10 nm nanoelectronic device research,[4] and mask manufacturing.[5] Achieving the highest possible resolution of EBL is important for these applications. Recent progress has been made in ultrahigh-resolution EBL with the emergence of new tools,[6] resists,[7–10] and processes.[11–14] For example, sub-5 nm half-pitch features have been reported using a Raith150-TWO EBL system with a salty-development process using hydrogen silsesquioxane (HSQ) resist.[6] However, fundamental questions still remain about the resolution limit of EBL. A better understanding of these fundamentals could enable further improvements in the resolution of EBL. To address these issues, we need to image and measure nanostructures accurately at sub-10 nm dimensions. However, at such small length scales, metrology becomes challenging.[15,16] For example, considering a critical-dimension control standard deviation of 10% for sub-5 nm half-pitch features implies a metrology accuracy of ~0.1 nm, which poses a challenge to even the best scanning electron microscopes (SEMs).

Transmission-electron microscopy (TEM) has the highest lateral resolution of any existing metrological method, and it has been extensively used in nanofabrication[17,18] and in the semiconductor manufacturing industry[19] for measuring the critical dimension of lithographic features, the accuracy of feature placement, and the thickness of functional layers (by cross-section imaging). On the other hand, atomic-force microscopy (AFM) has the highest vertical resolution of any known metrological technique. With its intrinsic advantage over TEM and SEM of operation in ambient condition, AFM has been used for measuring the diameter of nanoparticles[20] and quasi-one-dimensional structures.[21]

In this report, with the use of TEM, AFM, and SEM, we found that the feature size defined by EBL could be as small as 4 nm, but dense features with a half-pitch less than 8 nm were difficult to yield even with a high-contrast development process. To explain these results, we first measured the line-spread function (LSF) and the point-spread function (PSF) of the EBL using TEM. Then, we calculated that the image contrast in dense patterns was sufficiently high, and therefore the beam spot size and proximity effects did not limit the resolution of EBL in our case. We thus hypothesize that the resolution of EBL was primarily limited by the development process at the sub-10 nm half-pitch scales.

II. EXPERIMENTS AND METROLOGY STRATEGY

To use TEM and AFM to measure the dimension of electron-beam-defined features, the sample preparation process was different from that for SEM metrology. For TEM metrology, the substrate had to be thin enough to be transparent to electrons. Additionally, AFM measurements of lat-

[a)]Present address: Institute of Materials Science and Engineering, Agency for Science, Technology and Research, 3 Research Link, Singapore 117602, Singapore.
[b)]Electronic mail: berggren@mit.edu

Author complimentary copy. Redistribution subject to AIP license or copyright, see http://jvb.aip.org/jvb/copyright.jsp

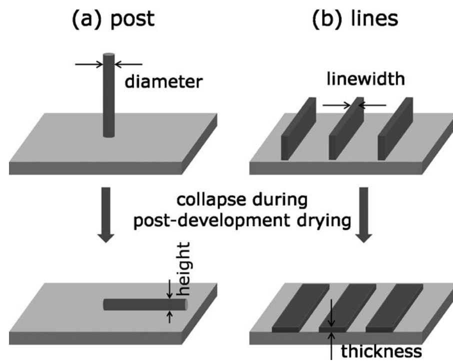

FIG. 1. Schematic diagram showing the method used to measure the lateral dimensions of isolated (a) posts and (b) lines by converting lateral measurements to accurate vertical measurements.

eral dimensions are inaccurate due to tip convolution effects. Therefore, special sample preparation processes were required to collapse features and convert feature width to accurate height measurements. We describe the sample preparation and metrological strategies below.

A. Electron-beam lithography

HSQ (XR1541) was adopted as the electron resist for the study. Electron-beam lithography was done using a Raith 150 with an accelerating voltage of 30 kV, an aperture size of 20 μm (corresponding to a beam current of ~180 pA), and a working distance of ~6 mm. After lithography, samples were developed using a salty-development process (1% NaOH+4% NaCl, 4 min, 24 °C)[11] and rinsed in deionized water. To study and analyze the resolution limit of electron-beam lithography, we fabricated both sparse and dense features and measured the point-/line-spread functions. To obtain the highest resolution features, the dose for both sparse posts/lines and dense nested Ls was optimized. Samples for TEM metrology were fabricated on freestanding 50-nm-thick low-stress silicon nitride (nonstoichiometric, close to SiN) membrane substrates (3 mm diameter, bought from Ted Pella Corp.), and those for AFM and SEM metrology were fabricated on silicon (100) substrates.

B. TEM metrology

TEM metrology was done by using a JEOL JEM 2010F microscope in the bright field mode with an accelerating voltage of 200 kV. Collapsed high-aspect-ratio (~20:1) HSQ posts were imaged to obtain the resolution limit of isolated dots, and nested Ls (the HSQ thickness was ~20 nm) were imaged to get the resolution limit of dense structures. Considering the background signal caused by silicon nitride membrane substrates, a minimal objective aperture size and a slight underfocus were used to enhance the image contrast of the exposed structures when imaging.

C. AFM metrology

The AFM measurement strategy is shown in Fig. 1. We fabricated very high-aspect-ratio (~20:1) features by electron-beam lithography exposures of a thick resist (~100 nm). These high-aspect-ratio structures naturally fell over or collapsed during the postdevelopment drying process. As shown in Fig. 1, this collapse turned a vertical post into a horizontal rod and a vertical line into a rectangular area. Thus, we could measure the height of the rod to obtain the diameter of the original post and the thickness of the lateral rectangular area to obtain the linewidth of the original line. AFM was done by using a DI Dimension-3000 microscope in the tapping mode.

III. RESULTS AND DISCUSSION

We show the measured highest resolution of sparse posts/ lines and dense nested Ls in this section. To analyze the resolution limiting factors of high-density structures, we used the point-/line-spread function to calculate the dose modulation in our designed patterns.

A. Measurement of sparse features

Figure 2 shows representative SEM, TEM, and AFM images of different fallen-over HSQ posts. From the SEM image (a), we know that the HSQ feature was very small, but we cannot obtain the exact feature size due to the blurring of feature edges. The edge blur of the SEM image was caused by the finite beam size and electron interaction volume in the material, which cannot be eliminated. Hence, it is difficult to obtain sub-1 nm measurement accuracy by SEM. In contrast, Fig. 2(b) shows the TEM image of a HSQ post fabricated with the same dose as in Fig. 2(a) (15 fC, ~94 000 electrons), in which we can clearly see the edges of this fallen-over post and thus obtain its dimension of ~4 nm. The measurement accuracy from this TEM image can approach 0.1 nm, as suggested by Fig. 2(b). Figure 2(c) gives a TEM image of a fallen-over HSQ post with a higher dose (20 fC, ~124 000 electrons), from which we obtained the diameter of the HSQ post of 5.5 nm. This larger post scattered more incident electrons, leading to a higher signal to noise ratio than in Fig. 2(b). Thus, we can see a better image contrast. In Figs. 2(b) and 2(c), the shape of the rods corresponds to the cross sections of the high-aspect-ratio posts, which contain information on the forward scattering angle of the electron beam as it enters the resist. The diameter of the post was very uniform along the entire post, which puts an upper limit on the forward scattering angle of the beam of ~10 mrads. Figure 2(d) shows an AFM image of a fallen-over HSQ array of posts fabricated with the same dose as Fig. 2(c) (20 fC), from which we can determine the diameter of HSQ posts to be ~5.6 nm. This measured diameter matches closely with that from TEM metrology [Fig. 2(c)].

Figure 3 shows the AFM measurement of fallen-oven high-aspect-ratio (>20:1) HSQ lines with a dose of 9 nC/cm (~5600 electrons/nm). By measuring the thickness of fallen-over lines, we can obtain the linewidth of original HSQ lines of ~3.8 nm, which strengthens the claim that sub-4 nm sparse features can be achieved using EBL. Comparing to TEM and SEM metrology, this AFM metrological strategy provides a more convenient way to measure the di-

Author complimentary copy. Redistribution subject to AIP license or copyright, see http://jvb.aip.org/jvb/copyright.jsp

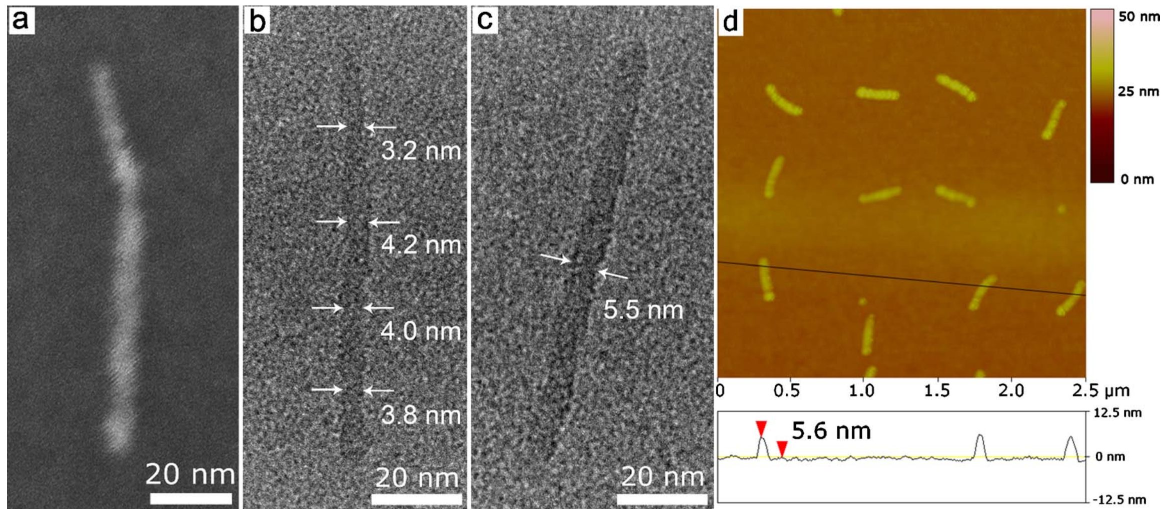

FIG. 2. (Color online) Images of fallen-over high-aspect-ratio HSQ posts fabricated using a Raith 150 EBL system at 30 kV followed by a salty-development process (1% NaOH+4% NaCl, 4 min, 24 °C). (a) SEM image of a post with dose of 15 fC ($\sim 9.4\times 10^4$ electrons); [(b) and (c)] TEM micrographs of HSQ posts with doses of 15 and 20 fC ($\sim 1.2\times 10^5$ electrons), respectively; (d) AFM image of HSQ post array with dose of 20 fC/post. The substrates for SEM and AFM metrologies were silicon, and those for TEM metrology were 50-nm-thick silicon nitride membranes. The thickness of HSQ was ~100 nm. The beam current was ~180 pA, corresponding to a spot size ~4 nm. The SEM was taken in the Raith 150 with an accelerating voltage of 10 kV and a working distance of ~6 mm; bright field TEM was done in a JEOL JEM 2010F tool with an accelerating voltage of 200 kV; AFM was done in a DI Dimension-3000 tool in tapping mode.

mensions of ultrasmall features because it can be done in ambient condition; i.e., no high vacuum is required. The drawback of this AFM metrology is that it is an indirect measurement method that requires collapse of features.

B. PSF and LSF measurements

PSF and development contrast are the two most important factors that determine the resolution of EBL. To analyze the resolution limit of EBL or to correct for proximity effect, the PSF must be accurately measured especially within the 10 nm radius from the center of exposure. With the use of accurate TEM metrology, we experimentally measured the PSF down to a 3 nm radius. The PSF was determined by plotting 1/dose versus the measured feature radius, as described in Ref. 22. With a similar method (but using a linewidth instead of a feature radius), LSF was also measured, which could be used to analyze the resolution limit of parallel-line patterns.

Figure 4 shows the measurement results of PSF (a) and LSF (b). We also did Monte Carlo simulation[23] for PSF and LSF, as shown by the dashed lines in the figures. Monte Carlo simulated PSF and LSF were in good agreement with the experimental data.

Data fitting of the PSF and LSF was done to extract analytic functions that can be used for dose-distribution and proximity-effect calculations. The phenomenological equation consisting of a sum of two Gaussians and a hyperbolic function was found to fit the data well for exposure at 30 kV.[24] In our case, the backscattering of electrons in the 50-nm-thick freestanding SiN membrane was negligible. Hence, we further simplified our analytical function, using only a single Gaussian to describe the forward-scattered electrons, and a hyperbolic function. The fitted formulas are shown in the insets of Figs. 4(a) and 4(b), and the fitting curves matched well with the measured and simulated data. It should be noted that the parameter α in PSF is an indicator of "forward scattering distance" in electron-beam lithography, while the parameter δ in LSF has no obvious physical meaning and is only a fitting parameter in this case, so their values are not comparable.

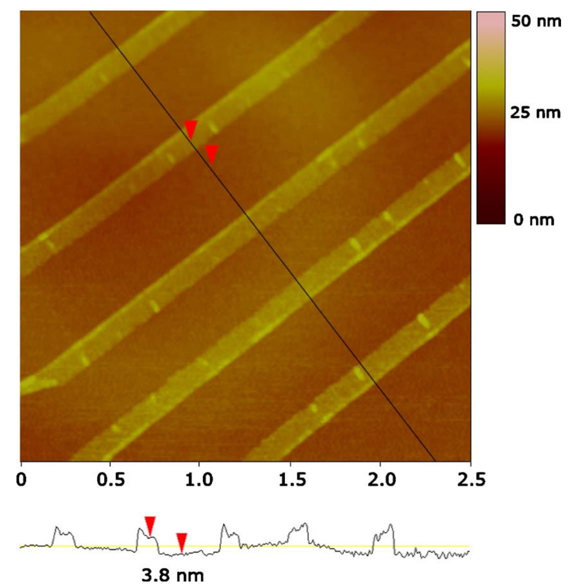

FIG. 3. (Color online) AFM image of fallen-over HSQ lines. The thickness of HSQ was ~100 nm, the pitch of designed lines was 500 nm, and the line dose was 9 nC/cm (5600 electrons/nm). All other lithography and development parameters were same as those indicated in Fig. 2. The AFM was done in a DI Dimension-3000 tool in tapping mode. Bottom: section profile along the indicated line.

Author complimentary copy. Redistribution subject to AIP license or copyright, see http://jvb.aip.org/jvb/copyright.jsp

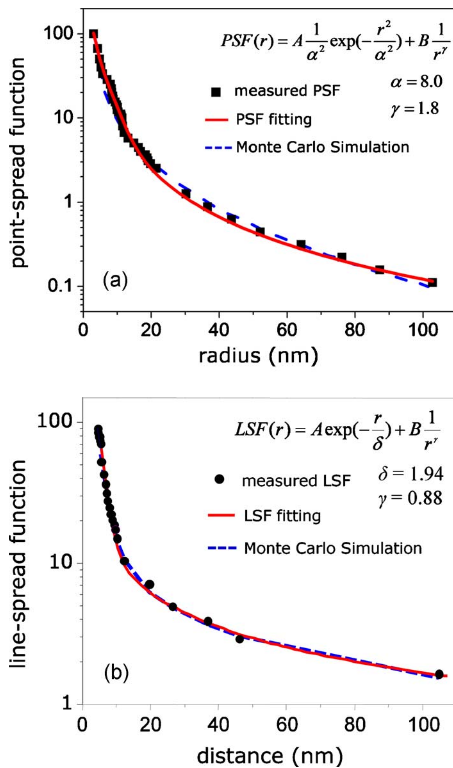

FIG. 4. (Color online) (a) PSF and (b) LSF measured by TEM on 50-nm-thick SiN membrane substrate with an accelerating voltage of 30 kV, their analytically fitted curves (solid lines), and Monte Carlo simulated curves (dashed lines). The PSF measurement was done on ~120-nm-thick HSQ, while the LSF was measured on ~20-nm-thick HSQ. The measurement method was the same as that described in Ref. 22. The unit of the parameter α in PSF and δ in LSF is nanometer. For simulations, the parameters are listed below: 30-nm-thick HSQ, 50-nm-thick SiN membrane substrate, 30 kV exposure voltage, 4 nm spot size, and 50 000 000 incident electrons, including secondary electrons.

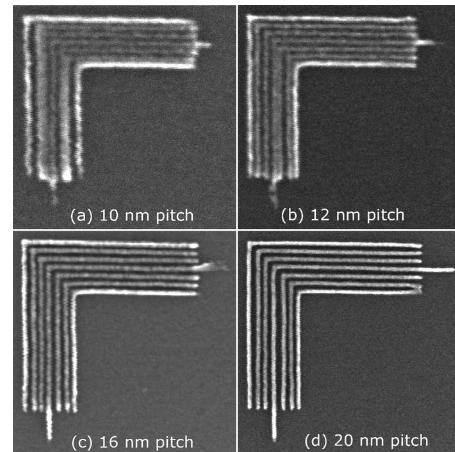

FIG. 5. SEM images of HSQ nested Ls from 10 to 20 nm pitches fabricated by using a Raith 150 EBL system at 30 kV and a salty-development process. The corresponding line doses were (a) ~4000, (b) ~4400, (c) ~5000, and (d) ~6300 electrons/nm. The thickness of HSQ was 26 nm. The aperture was 20 μm, corresponding to a beam current of ~180 pA and a spot size of ~4 nm.

C. Resolution limit of dense structures

High-density structures are more interesting and important than isolated structures in manufacturing high-density magnetic storage media,[1,13] integrated circuits, and superconducting nanowire single photon detectors.[25] However, fabrication of high-density structures is much more difficult than the fabrication of sparse features due to the proximity effect induced by nonideal initial beam spot sizes, forward scattering electrons, secondary electrons, and backscattering electrons. To investigate the resolution limit for patterning high-density structures, we used nested-L patterns with varying pitches.

Figure 5 shows SEM images of high-resolution-EBL results for nested-L patterns ranging from 10 to 20 nm pitches. We can see that 20 nm pitch HSQ structures were well resolved and that 10 nm pitch structures were also resolvable. However, there are two issues with these SEM images: (1) The feature sizes cannot be accurately measured, and (2) the quality of fabricated dense structures, such as the presence of footing/bridging between the lines, cannot be determined. These issues are critical in real applications, but SEMs do not provide sufficient information to answer these questions.

To address above-mentioned issues, we fabricated nested Ls on membrane substrates and used TEM to characterize them. Figures 6(a)–6(d) show TEM micrographs of HSQ nested Ls from 10 to 20 nm pitches, from which we can confirm that 20 nm pitch structures were well-defined and 10 nm pitch structures were still resolvable. It should be noted here that the features on the membrane [Fig. 6(d)] tended to collapse though their aspect ratio was not as high as these on a silicon substrate [Fig. 5(d)], which might be caused by the adhesion problem between HSQ and SiN membranes or the deformation mismatch of HSQ and SiN. With the high measurement accuracy of TEM, we obtained the accurate feature size of HSQ lines, as indicated in Fig. 6(c), where a 4 nm linewidth was obtained in 16 nm pitch HSQ nested Ls.

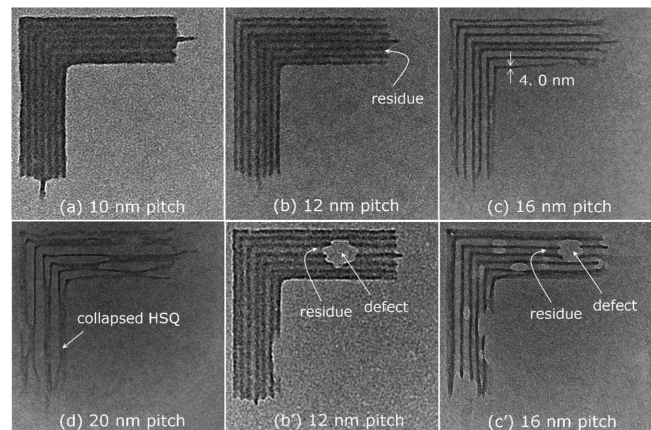

FIG. 6. Bright field TEM micrographs of HSQ nested Ls with varying pitch: (a) 10 nm, [(b) and (b′)] 12 nm, [(c) and (c′)] 16 nm, and (d) 20 nm. The thickness of HSQ was about 18 nm, and the substrate was 50-nm-thick silicon nitride membrane. All other EBL parameters were same as those in Fig. 5. TEM was done in a JEOL JEM 2010F tool with an accelerating voltage of 200 kV.

Author complimentary copy. Redistribution subject to AIP license or copyright, see http://jvb.aip.org/jvb/copyright.jsp

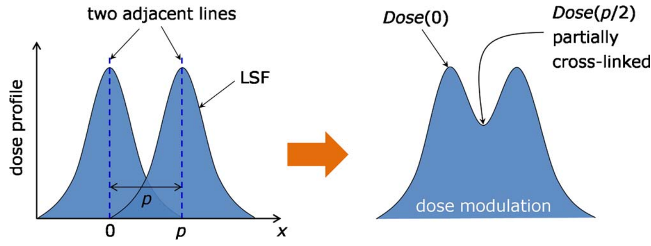

FIG. 7. (Color online) Schematic illustrating the overlap of two line-spread functions of two adjacent lines (left) and the formation of dose modulation resulting in partial cross-linking of spacing area between them (right).

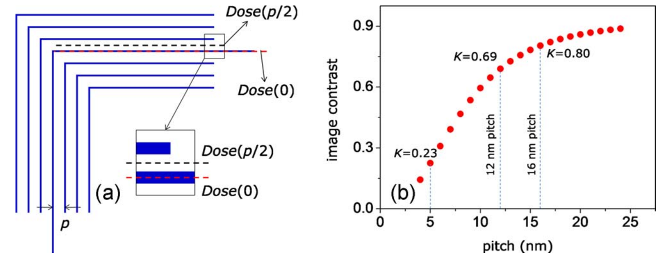

FIG. 8. (Color online) (a) Schematic diagram to illustrate the dose distribution at the original position and the center of two lines in designed nested-L structures; (b) image contrast of dose distribution K as a function of pitch.

Meanwhile, the TEM micrographs also showed resist residues between the lines, which could not be seen in the SEM images.

To further study the residue between the designed features, we selected defective HSQ films (due to the dewetting during the spin-coating process) for exposure. Representative results are shown in Figs. 6b′ and 6c′. With the help of defects, the image was more easily interpreted, so we could evaluate the residues between the designed features. For example, from Fig. 6c′, we see that the residues exist in 16 nm pitch HSQ features, which means that 16 nm pitch structures were difficult to completely resolve at our exposure and development conditions. For smaller pitches, more residues were evident, as shown in Fig. 6b′ (12 nm pitch), which indicates that these structures were more difficult to resolve.

D. Analysis and discussion

As seen in the above results, sub-4 nm sparse HSQ features were fabricated by EBL, but dense 16 nm pitch structures were difficult to yield. Generally, poor latent-image contrast due to proximity effects, i.e., the overlap of PSFs, was considered to be the reason for this difference. But we argue below that proximity effect alone could not explain the residue in between the lines, and that some additional affect—possibly a pattern-dependence of development rates—was responsible.

Consider the exposure dose profile of two adjacent lines, as shown in the left schematic in Fig. 7. The resultant dose profile is the sum of the LSFs of the individual lines, as shown in the right schematic. Hence, the area between the two lines will be partially exposed due to electron scattering. Setting the origin of the x-axis at the left line and defining p as the separation between lines, the dose maxima dose(0) and dose(p) occur at $x=0$ and p, respectively, and the dose minimum dose($p/2$) is in between the lines at $x=p/2$. When the dose($p/2$) is larger than the onset dose (for the negative resist, the onset dose is defined as the minimum dose at which the resist remaining after the development is not zero), there will be a residue between the lines. Both dose(0) and dose($p/2$) are functions of exposure dose and line separation p.

Because we have already measured the LSF [as shown in Fig. 4(b)], we can calculate both dose(0) and dose($p/2$) as a function of pitch p at a given original deposited dose. Extending the calculation to the nested-L pattern and defining dose(0) as the dose of the middle line, as illustrated in Fig. 8(a), we can calculate the maximum dose dose(0) and its adjacent minimum dose dose($p/2$) as follows:

$$\text{dose}(0) = D + 2D \times \text{LSF}(p) + 2D \times \text{LSF}(2p) + 2D \times \text{LSF}(3p),$$

$$\text{dose}(p/2) = 2D \times \text{LSF}(p/2) + 2D \times \text{LSF}(3p/2) + 2D \times \text{LSF}(5p/2) + D \times \text{LSF}(7p/2),$$

where D is the exposure line dose and LSF is line-spread function, as illustrated in Fig. 4(b). $\text{LSF}(r)=A\exp(-r/\delta)+B(1/r^{\gamma})$, in which $A=736$, $B=109$, $\delta=1.94$, and $\gamma=0.88$. Image contrast K defined as $K=(\text{dose}(0)-\text{dose}(p/2))/(\text{dose}(0)+\text{dose}(p/2))$ is used to describe the amount of dose modulation. Better contrast (i.e., larger K) results in better resolvability. By calculation, we could obtain the image contrast, as shown in Fig. 8(b), from which we can see that the image contrast increases as the pitch is increased; i.e., it is easier to resolve sparser structures than to resolve dense structures, as observed qualitatively in the experiments. But it turns out that a quantitative analysis predicts less footing to occur than we actually observe.

With the image contrast K, we can analyze the resolvability of different pitch structures. Using 16 nm pitch HSQ structures as an example, K was calculated to be ~0.8 based on the measured LSF, as indicated in Fig. 8(b). With this image contrast, we can calculate the dependence of dose($p/2$) on dose(0), shown in Fig. 9. Defining the onset dose to be D_{o} and the threshold dose to be D_{t} (at which the remaining thickness of resist in a macroscopic measurement would be 75% of the maximum remaining), from the salty-development contrast curve (see Ref. 11, as also illustrated in the inset of Fig. 9), D_t is estimated to be about $1.5D_o$.

If we use a working dose D_w, which makes $\text{dose}(0)>D_t$ and $\text{dose}(p/2)<D_o$ (see the line segments indicated in a 16 nm pitch line), by a conventional model we should expect to obtain resolved structures. For example, in our experiment for the 16 nm pitch HSQ structure, as shown in Fig. 7c′, the working dose D_w was $\sim 2D_t$ (D_w was 8 nC/cm, while the onset dose was ~4 nC/cm), so 16 nm pitch structures should be clearly resolved; i.e., no residue was predicted to remain. Using the same analysis process, 12 nm pitch structures should also be clearly resolved. Moreover, if we can use a working dose D_w exactly equal to D_t, a 5 nm pitch

Author complimentary copy. Redistribution subject to AIP license or copyright, see http://jvb.aip.org/jvb/copyright.jsp

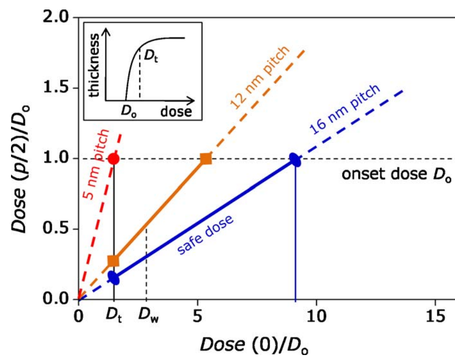

FIG. 9. (Color online) Schematic diagram of the relationship dose$(p/2)/D_o$ as a function of dose$(0)/D_o$ for pitches of 16, 12, and 5 nm. Inset is the schematic diagram (not actual data) of the development contrast curve for HSQ by a salty-development process for 4 min at 24 °C. D_o, D_t, and D_w represent onset dose, threshold dose, and working dose, respectively, where $D_t = \sim 1.5D_o$ obtained from the contrast curve. The line segments in 16 and 12 nm pitch plots were the expected safe-dose regions (or process windows) for resolved structures. The 5 nm pitch plot suggests that a process window does not exist for this pitch, and so 5 nm pitch might be the theoretical limit of this lithographic process, assuming a perfect development process.

could be resolvable. However, in our experiments, a 20 nm pitch pattern was the minimum clearly resolved dimension, a residue was observed in the 16 nm pitch HSQ structures, much residue was observed in the 12 nm pitch HSQ structures, and sub-10 nm pitch structures were almost unresolvable. These experimental results suggest that our analysis model is incomplete.

Two sets of data were used in the above analysis. One was a dose-distribution calculation by using the measured line-spread function, and another was a resist-thickness-remaining calculation by using a measured development contrast curve. The dose distribution was reliable because it was calculated from experimental data. The development contrast curve was also measured, but only on 10 μm scale structures.[11] The problem may be that 10 μm scale development-rate data do not describe small-scale high-density structure development. This effect can be understood because the actual development process in dense structures occurred in sub-10 nm grooves, and the development mechanism under this confinement could conceivably be quite different from that in micron-scale structures.

To explain the residue in 16 nm pitch HSQ structures, we propose a hypothesis below. The dose modulation in dense structures led to partially cross-linked HSQ in the spacing between the designed lines. At nanoscale spacings, nanogrooves will form in the early development process. The developer may have difficulty diffusing into the nanogrooves to further develop the partially cross-linked HSQ due to possible surface charging effects,[6] or developed HSQ material may have difficulty diffusing out of the nanogrooves, so the development speed would slow down due to mass-transport limitations.[15] These mass-transport limitations would result in an incomplete development of partially cross-linked HSQ, so residues were not removed.

IV. CONCLUSION

We adopted transmission-electron microscopy and atomic-force microscopy to improve the metrological accuracy and analyze the resolution limit of electron-beam lithography. With better metrology, we found that sub-5 nm sparse features could be readily fabricated by electron-beam lithography, but dense 16 nm pitch structures were difficult to yield. By using experimental point- and line-spread functions for analysis, we inferred that the resolution in fabricating sub-10 nm half-pitch ultrahigh-density features was primarily limited by the resist-development process.

ACKNOWLEDGMENTS

The authors thank Henry I. Smith, James M. Daley, and Mark K. Mondol for helpful discussions and Juan Ferrera for providing PSF Monte Carlo simulation codes. Electron-beam lithography was done in MIT's shared scanning-electron-beam-lithography facility in the Research Laboratory of Electronics. H.D. would like to acknowledge his partial fellowship from China Scholarship Council. V.R.M. was supported as part of the Center for Excitonics, an Energy Frontier Research Center funded by the U.S. Department of Energy, Office of Science, Office of Basic Energy Sciences under Award No. DE-SC0001088. This work was also supported in part by the Information Storage Industry Consortium, Nanoelectronics Research Initiative, the NSF.

[1] B. D. Terris and T. Thomson, J. Phys. D: Appl. Phys. **38**, R199 (2005).
[2] I. Bita, J. K. W. Yang, Y. S. Jung, C. A. Ross, E. L. Thomas, and Karl K. Berggren, Science **321**, 939 (2008).
[3] J. K. W. Yang, Y. S. Jung, J. B. Chang, R. A. Mickiewicz, A. Alexander-Katz, C. A. Ross, and K. K. Berggren, Nat. Nanotechnol. **5**, 256 (2010).
[4] Z. Chen, Y. M. Lin, M. J. Rooks, and P. Avouris, Physica E (Amsterdam) **40**, 228 (2007).
[5] W. Wu *et al.*, Nano Lett. **8**, 3865 (2008).
[6] J. K. W. Yang, B. Cord, H. G. Duan, J. Klingfus, S. W. Nam, K. B. Kim, M. J. Rooks, and K. K. Berggren, J. Vac. Sci. Technol. B **27**, 2622 (2009).
[7] H. Sailer, A. Ruderisch, D. P. Kern, and V. Schurig, J. Vac. Sci. Technol. B **20**, 2958 (2002).
[8] M. S. M. Saifullah, K. R. V. Subramanian, E. Tapley, D. J. Kang, M. E. Welland, and M. Butler, Nano Lett. **3**, 1587 (2003).
[9] M. S. M. Saifullah, K. R. V. Subramanian, D. J. Kang, D. Anderson, W. T. S. Huck, G. A. C. Jones, and M. E. Welland, Adv. Mater. **17**, 1757 (2005).
[10] X. Chen, R. E. Palmer, and A. P. G. Robinson, Nanotechnology **19**, 275308 (2008).
[11] J. K. W. Yang and K. K. Berggren, J. Vac. Sci. Technol. B **25**, 2025 (2007).
[12] B. Cord, J. Lutkenhaus, and K. K. Berggren, J. Vac. Sci. Technol. B **25**, 2013 (2007).
[13] X. M. Yang, S. Xiao, W. Wu, Y. Xu, K. Mountfield, R. Rottmayer, K. Lee, D. Kuo, and D. Weller, J. Vac. Sci. Technol. B **25**, 2202 (2007).
[14] S. Yasin, D. G. Hasko, and H. Ahmed, Appl. Phys. Lett. **78**, 2760 (2001).
[15] B. Cord, J. K. W. Yang, H. G. Duan, D. C. Joy, J. Klingfus, and K. K. Berggren, J. Vac. Sci. Technol. B **27**, 2616 (2009).
[16] S. Knight, R. Dixson, R. L. Jones, E. K. Lin, N. G. Orji, R. Silver, J. S. Villarrubia, A. E. Vladár, and W. L. Wu, C. R. Phys. **7**, 931 (2006).
[17] S. Choi, M. Yan, L. Wang, and I. Adesida, Microelectron. Eng. **86**, 521 (2009).
[18] W. F. van Dorp, B. van Someren, C. W. Hagen, and P. Kruit, Nano Lett. **5**, 1303 (2005).

Author complimentary copy. Redistribution subject to AIP license or copyright, see http://jvb.aip.org/jvb/copyright.jsp

[19]R. B. Marcus and T. T. Sheng, *Transmission Electron Microscopy of Silicon VLSI Circuits and Structures* (Wiley, New York, 1983), Vol. 1, pp. 1–217.
[20]G. Wilkening and L. Koenders, *Nanoscale Calibration Standards and Methods* (Wiley-VCH, Weinheim, 2006), Vol. 1, pp. 359–374.
[21]A. Javey and H. Dai, J. Am. Chem. Soc. **127**, 11942 (2005).
[22]R. Menon, D. Gil, and H. I. Smith, J. Opt. Soc. Am. A **23**, 567 (2006).
[23]Based on the codes in R. A. Ghanbari, Ph.D. thesis, Massachusetts Institute of Technology, 1993.
[24]L. Battistella, D. Winston, J. Ferrera, and K. K. Berggren unpublished work.
[25]J. K. W. Yang, A. J. Kerman, E. A. Dauler, B. Cord, V. Anant, R. J. Molnar, and K. K. Berggren, IEEE Trans. Appl. Supercond. **19**, 318 (2009).

Author complimentary copy. Redistribution subject to AIP license or copyright, see http://jvb.aip.org/jvb/copyright.jsp